RESEARCH ARTICLE

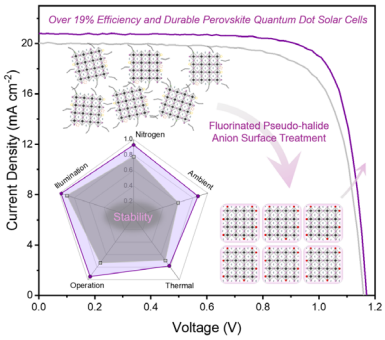

A pseudo-halide, short-chain, and hydrophobicity anion PF_6^- is introduced to form a ligand shell of $FAPbI_3$ perovskite quantum dot (PQD) to overcome surface defect density, inter-dot transport, and instability challenges, output a record-high efficiency of over 19% and improve long-term stability in PQD solar cells.

ADVANCED MATERIALS
www.advmat.de

Fluorinated Pseudo-Halide Anion Enables >19% Efficiency and Durable Perovskite Quantum Dot Solar Cells

*Chenyu Zhao, Du Li, Xuliang Zhang, Hehe Huang, Claudio Cazorla, Xinyu Zhao, Huifeng Li, Yuhao Chen, Wei Zhu, Tom Wu, and Jianyu Yuan**

Metal halide perovskite quantum dots (PQDs), like formamidinium lead triiodide ($FAPbI_3$), hold significant promise for next-generation photovoltaics. Surface manipulation of PQDs has been extensively reported to be crucial to their photovoltaic performance due to the dynamic binding of capping long-chain ligands. In this work, an efficient surface engineering strategy employing a multifunctional fluorinated pseudo-halide anion ligand, hexafluorophosphate (PF_6^-) is reported for achieving efficient $FAPbI_3$ PQD solar cells. Leveraging its coordination capability, large ionic radius (2.38 Å), and intrinsic hydrophobicity, PF_6^- simultaneously passivates iodide vacancies, minimizes inter-dot spacing for enhanced electronic coupling, suppresses ion migration, and provides a hydrophobic barrier. By replacing oleate ligands with PF_6^- in $FAPbI_3$ PQDs, an unprecedented high efficiency of 19.01% (17.19% for a 1 cm^2-sized device) is achieved, and enhanced storage and operational stability. These findings will provide insight into the design of robust surface structures and low-trap-states PQD films toward high-efficiency and stable solar cells.

1. Introduction

Metal halide perovskite quantum dots (PQDs), with their unique size-tunable properties and excellent solution processability, have emerged as promising candidates for next-generation optoelectronic devices.[1–3] For the photovoltaic application, PQD solar cells have achieved remarkable progress from 10.77% to over 18%, surpassing all other colloidal quantum dot materials.[4–6] More importantly, the high specific surface area and surface chemistry engineering would provide new platforms to solve the humidity, temperature, and light-related instability issues buried in the bulk thin-film perovskite.[7] These theoretical benefits require additional research to find either the best composition or surface chemistry environment of PQDs or engineer the entire device system toward both high efficiency and better stability to finally push this technology forward.[8–10]

The colloidal synthesis of PQDs inherently relies on long-chain insulating ligands (e.g., oleic acid (OA) and oleylamine (OAm)) to stabilize nanocrystal surfaces and prevent aggregation.[11–13] Due to the ionic nature of the perovskite structure, there is a dynamic adsorption–desorption process between these capping ligands and the PQD surfaces, thus generating many surface defects (e.g., iodide vacancies and dangling bonds), which can serve as non-radiative recombination centers.[14] Moreover, the long and insulating capping ligands would significantly hinder electronic coupling between adjacent PQDs, severely limiting charge transport across the quantum dot solids.[15–17] Attempts to totally remove these ligands during device fabrication often led to structural collapse and thus accelerated degradation, as the exposed surfaces become vulnerable to environmental moisture/oxygen attack.[18–20] Under the circumstances, the multi-interfacial architecture of PQDs would introduce ion-migration pathways.[21] The grain boundaries and interdot spaces formed during ligand stripping serve as pathways for halide (I^-/Br^-) and organic cation (formamidinium$^+$ (FA^+)/methylammonium (MA^+)) migration under operational biases, leading to phase segregation, device hysteresis, and undesired degradation.[21,22] Although in-depth research on ligand exchange/passivation strategies has promoted the rapid development of power conversion efficiency (PCE) of PQD solar cells, it is still challenging to overcome these charge transport obstacles while maintaining the robust surface nanostructure of PQDs.[23–25]

In this contribution, we propose a simple yet efficient surface engineering strategy employing a multifunctional fluorinated pseudo-halide anion ligand, hexafluorophosphate (PF_6^-), to resolve both charge transport and stability challenges. The PF_6^- anion integrates target functions through its unique structure: coordination capability, a large ionic radius (2.38 Å), and intrinsic hydrophobic properties.[26,27] The octahedral structure

C. Zhao, D. Li, X. Zhang, H. Huang, X. Zhao, H. Li, Y. Chen, W. Zhu, J. Yuan
State Key Laboratory of Bioinspired Interfacial Materials Science
Institute of Functional Nano & Soft Materials (FUNSOM)
Soochow University
199 Ren-Ai Road, Suzhou Industrial Park, Suzhou, Jiangsu 215123, China
E-mail: jyyuan@suda.edu.cn

C. Cazorla
Department de Física
Universitat Politècnica de Catalunya
Barcelona 08034, Spain

T. Wu
Department of Applied Physics
The Hong Kong Polytechnic University
Kowloon, Hong Kong 999077, China

The ORCID identification number(s) for the author(s) of this article can be found under https://doi.org/10.1002/adma.202512201

DOI: 10.1002/adma.202512201

and electronegativity of PF_6^- enable its multiple F atoms to form a weak coordination bond network with the adjacent perovskite structure, effectively passivating iodide vacancies and suppressing trap states. Simultaneously, the compact ligand shell formed by PF_6^- could minimize inter-dot spacing relative to conventional long-chain ligands, thereby enhancing electronic coupling. Furthermore, the steric bulk of PF_6^- would act as a physical barrier at PQDs interfaces, obstructing ion diffusion channels, while its fluorine-rich hydrophobic surface mitigates hydrolytic degradation. Ultimately, the PF_6^--engineered $FAPbI_3$ PQD solar cells exhibit enhanced photovoltaic efficiency and stability, achieving a champion PCE of 19.01% and retaining ≈90% of their initial efficiency after 200 h of continuous operation under 1-sun illumination.

2. Results and Discussion

The colloidal $FAPbI_3$ PQDs capped with long-chain OA and OAm ligands were prepared by the hot-injection method,[15] with details described in the Supporting Information. In this work, the $MAPF_6$ molecule was introduced into the anti-solvent (methyl acetate (MeOAc)) during the solution-phase ligand exchange process for surface treatment as described in the Experimental Section,[8] and the result PQDs serve as the target PQDs. The PQDs treated with only MeOAc served as the control PQDs. Both the control and target PQDs display an average size of ≈16 nm based on transmission electron microscopy (TEM) characterizations (Figure S1, Supporting Information). Figure S2 (Supporting Information) shows the UV–vis absorption and the Tauc plot of the PQDs, and both $FAPbI_3$ PQDs exhibit similar absorption edges and narrow band gaps (E_g) of ≈1.60 eV. During the ligand exchange process, low-polarity anti-solvents, MeOAc, could remove part of the capping OAm/OA ligands, as shown in **Figure 1a**.[4] Upon ligand detachment, unfortunately, surface V_{FA} and V_I vacancies will be generated owing to the ionic nature and weak FA^+-$[Pb_6]^{4-}$ bonding in perovskites, causing lattice distortion and instability.[19] To solve the trade-off of carrier transport and stability, we anticipated that the $MAPF_6$ could simultaneously fill the V_{FA} through MA^+, while the PF_6^- anion acts as a pseudo-halide anion to reduce the surface V_I. This dual-action would accelerate ligand exchange, preserve PQD uniformity/integrity, passivate surfaces, reduce trap density, and enhance stability. Density functional theory (DFT) calculations (Figure 1b; Figure S3, Supporting Information) reveal enhanced binding energy of PF_6^- (−2.11 eV) on $FAPbI_3$ surfaces than OA (−0.97 eV), demonstrating the passivation ability of PF_6^-, which contributes to an increase in photoluminescence quantum yield (PLQY) (Figure 1c). Steady-state photoluminescence (PL; Figure 1d) and time-resolved PL (TRPL; Figure 1e; Table S1, Supporting Information) further confirm enhanced passivation by $MAPF_6$. The target PQDs exhibit enhanced PL intensity and a prolonged average carrier lifetime.[29,30]

The surface chemistry environment of the control and target $FAPbI_3$ PQDs was then analyzed by Fourier-transform infrared (FTIR) and X-ray photoelectron (XPS). As displayed in Figure 1f, the FTIR spectra reveal a decrease in peak intensities at 2750–3000 cm^{-1} for the target PQDs compared to the control, which corresponds to the vibrational mode of $\nu(C\text{-}H_x)$ in OA and OAm, demonstrating effective replacement of OA/OAm ligands by $MAPF_6$.[31] Concurrently, the target PQDs show a weak vibration peak at 843 cm^{-1}, corresponding to the vibration of the −P—F group (Figure S4, Supporting Information), suggesting the existence of PF_6^- on the PQDs surface. The high-angle annular dark field transmission electron microscopy (HAADF-TEM) elemental mapping (Figure 1g) further confirms the spatial distribution of F and P atoms, supporting the introduction of PF_6^- ligand. This conclusion was further corroborated by the XPS characterization (Figure 1h; Figure S5, Supporting Information), the core level spectra signal corresponding to F 1*s* can be observed. Meanwhile, the Pb 4*f* and I 3*d* core level spectrum of target PQDs shifts to a higher binding energy relative to that of the control PQDs, suggesting interactions between F atoms and the Pb^{2+}/I^-.[28] In addition, the increased stoichiometric ratio of X (X = I^- or PF_6^-) to Pb elements for the target PQDs corroborates the coordination of the PF_6^- ions (Figure S6, Supporting Information). Moreover, the N 1*s* spectrum of the target PQDs shows an enhanced peak at 402.1 eV (—NH_3^+ from incorporated MA^+), indicating cation exchange between MA^+ and FA^+.[32] Meanwhile, the peak at 400.5 eV (—NH_2^+ from FA^+) slightly shifts toward higher binding energy, which may be attributed to the hydrogen bond interaction between PF_6^- and FA^+ (F···H—N).[26]

Next, we assessed how $MAPF_6$ ligand regulates nanoscale crystalline structure, surface topography, and its impact on the carrier dynamic process. The 2D grazing incidence wide-angle X-ray scattering (2D-GIWAXS) patterns provide insights into the crystallographic properties of PQD films. **Figure 2a** displays well-defined diffraction rings assigned to the (100), (110), (111), and (200) planes of the cubic perovskite phase, confirming high crystallinity and phase purity, which is consistent with the X-ray diffraction (XRD) data (Figure S7, Supporting Information). Azimuthal integration of the (100) peak (Figure 2b; Figure S8, Supporting Information) reveals a pronounced intensity enhancement at 90° for the target film, suggesting a strong vertical alignment of the (100) plane. This preferential orientation would facilitate directional charge transport perpendicular to the substrate, thereby minimizing recombination losses and optimizing photovoltaic efficiency.[33] Top-view scanning electron microscopy (SEM) images (Figure 2c) reveal enhanced morphological uniformity and less pinholes in the target PQD film. This improved uniformity is corroborated by atomic force microscopy (AFM) height profiles (Figure S9, Supporting Information), which show a reduced root-mean-square (RMS) roughness of 5.47 nm compared to the control film (6.80 nm). Kelvin probe force microscopy (KPFM) further visualizes the surface potential distribution of the PQD films (Figure S10, Supporting Information), demonstrating a narrower contact potential difference (CPD) distribution of the target film. Quantitatively, the average CPD of the target film is ≈50 mV lower than that of the control film (Figure 2d), suggesting that $MAPF_6$ effectively improves surface uniformity and reduces potential fluctuations, thereby facilitating more efficient interfacial charge transfer.[34] Furthermore, the conductivity characterization of the PQD films (Figure 2e) confirms the enhanced charge transport capability.[37]

To elucidate the carrier dynamics of different PQD films, 2D confocal PL mapping and TRPL characterizations were performed in a device structure of FTO/TiO_2/PQDs. The 2D PL mapping displays lower PL intensity in the target PQD film relative to that of the control ones (Figure 2f), indicating improved

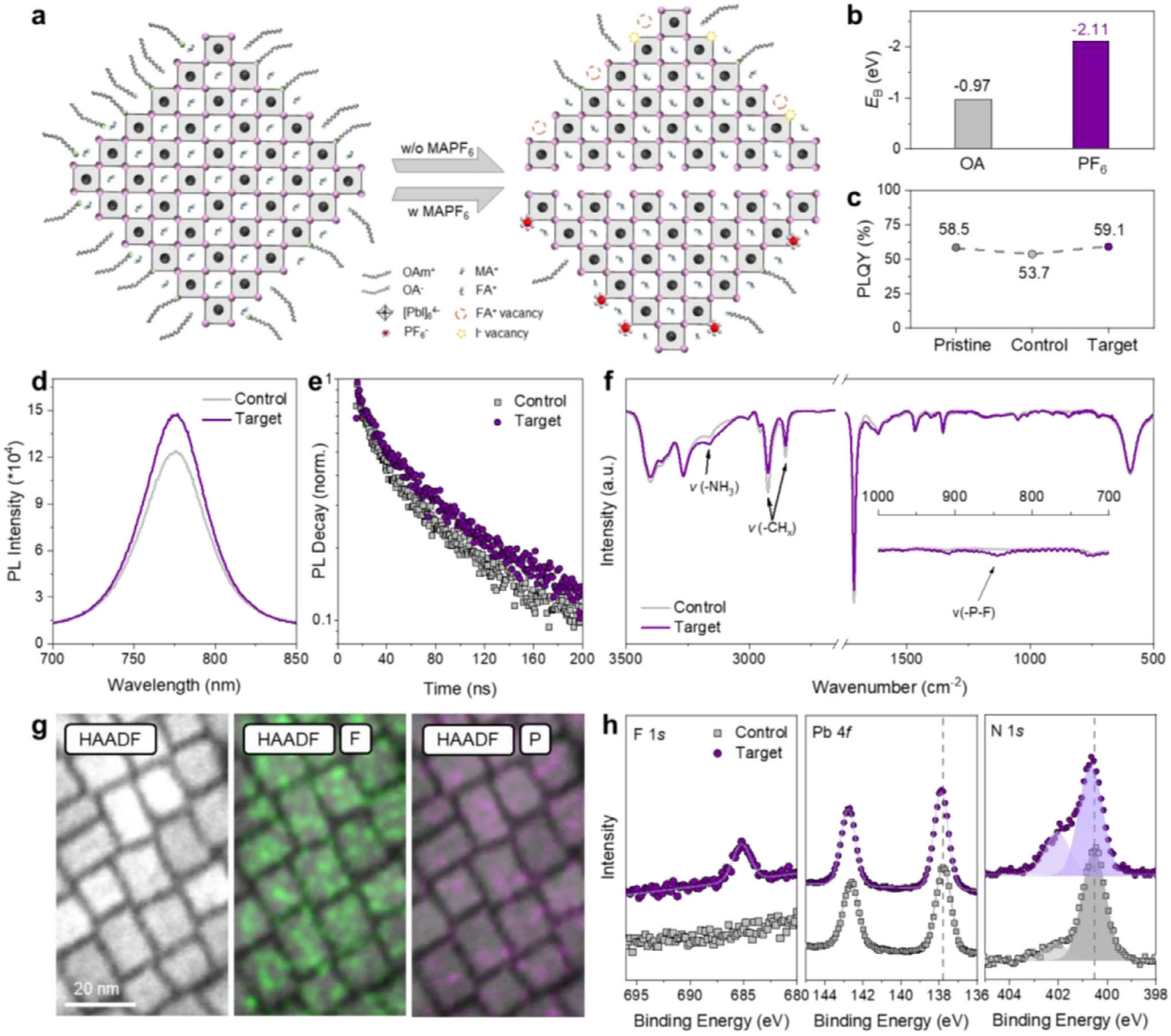

Figure 1. a) Schematic illustration of surface chemical environment of $FAPbI_3$ PQDs treated with and without $MAPF_6$. b) Binding energy difference by DFT methods for the equilibrium of OA and PF_6 on the $FAPbI_3$ structure. c) PLQY of pristine, control, and target $FAPbI_3$ PQDs. d) Steady-state PL spectra, e) TRPL spectra, and f) FTIR spectra of the control and target PQDs. g) HAADF-TEM elements mapping images of the target PQDs. h) F 1s, Pb 4*f*, and N 1s core-level XPS spectra of the control and target PQDs.

interfacial contact and enhanced charge extraction efficiency at the PQD/TiO_2 interface.[35] This was further verified by the TRPL measurement (Figure 2g), where the target PQD film demonstrates a reduced carrier lifetime of 5.42 ns, lower than that of the control film (5.89 ns, Table S2, Supporting Information).[36] Conversely, electron transport layer (ETL)-free structures show the target film has a longer lifetime (18.86 vs. 16.92 ns, Table S3, Supporting Information), signifying suppressed non-radiative recombination. The carrier diffusion distance (L_D) (Figure 2h) was further calculated based on the TRPL results,[37] and the target PQD film exhibits a longer L_D of 400.77 nm than that of the control film (348.47 nm). Femtosecond transient absorption (fs-TA) spectroscopy reveals the interfacial charge dynamics (Figure S11, Supporting Information). A distinct ground-state bleaching (GSB) signal centered at ≈755 nm (dashed white line) was observed, corresponding to the first excitonic transition. The fitting results in Figure 2i exhibit a prolonged trap-state recombination lifetime in the target PQD film compared to the control one (Table S4, Supporting Information), demonstrating mitigated non-radiative losses and enhanced charge separation efficiency.[37]

Then, we fabricated the planar n-i-p $FAPbI_3$ PQD solar cells with a device structure of Glass/FTO/TiO_2/$FAPbI_3$ PQDs/poly(triarsylamine) (PTAA)/MoO_3/Ag, as shown in **Figure 3a**. The concentration of $MAPF_6$ was optimized to be 0.05 mg mL^{-1} to achieve the best performance (Figure S12

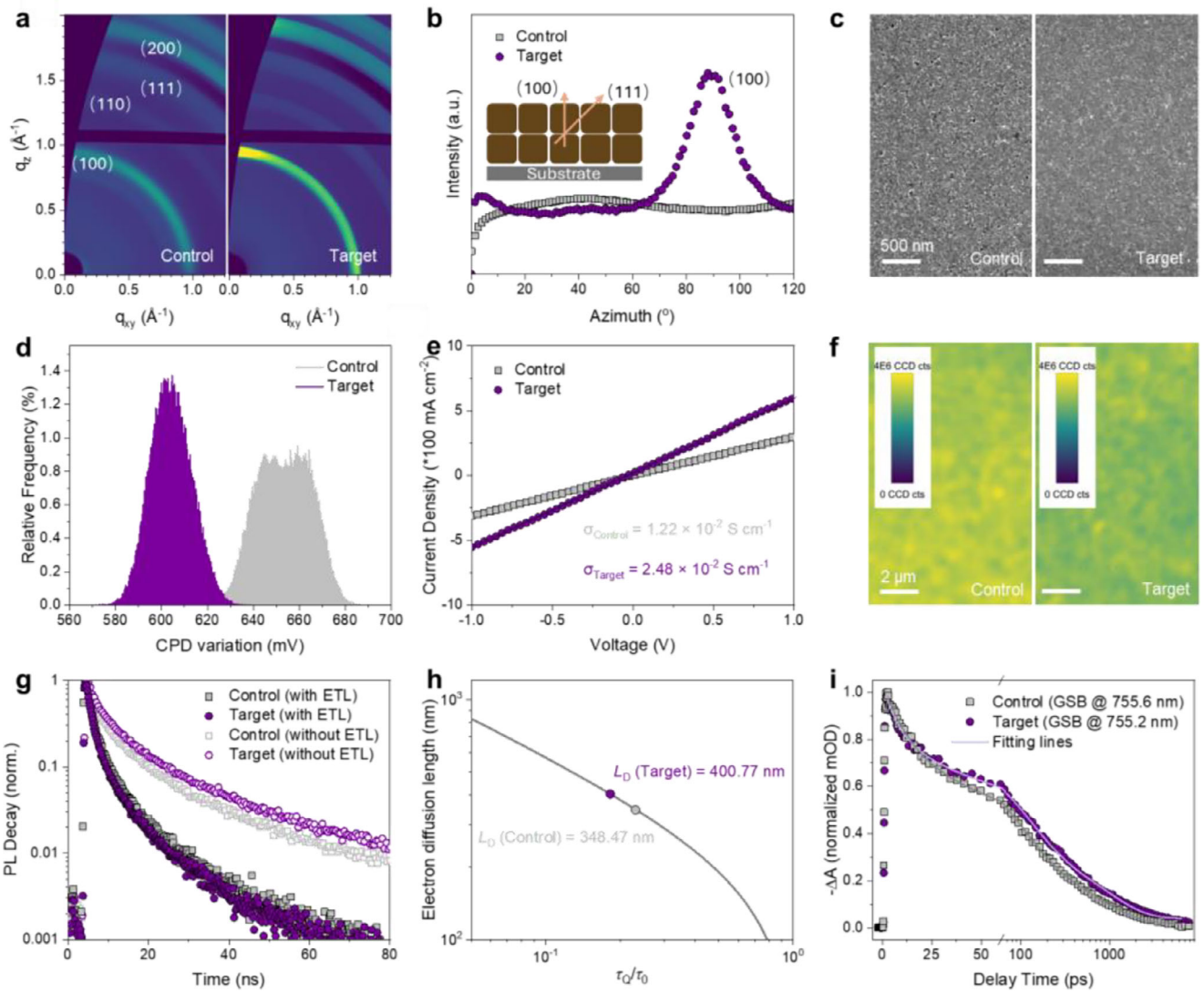

Figure 2. a) 2D-GIWAXS patterns and b) the corresponding (100) azimuthal integrations of the control and target PQD films. c) SEM images of different PQD films. d) Surface potential distributions of different PQDs films from KPFM images. e) Conductivity measurement of different PQD films. f) PL mapping images of different PQD films. g) TRPL spectra of different PQD films w/wo transport layer. h) Electron diffusion length calculation of different PQD films. i) The corresponding GSB decay spectra of different PQD films from TA spectra.

and Table S5, Supporting Information). The surface chemical properties of PQD may affect its band structure.[8] Therefore, the UV photoelectron spectroscopy (UPS) (Figure S13, Supporting Information) was introduced to determine its energy levels, with the results shown in Figure 3b. In comparison with the control PQDs, the conduction band and valence band of the target PQDs show an upward shift, forming a more favorable energy level alignment with the charge transport materials for charge extraction.[38] Figure 3c shows the current density–voltage (J–V) scans of the best performing control and target devices under AM 1.5G simulated solar illumination. For the control device, the optimal device displays a PCE of 17.23% with an open circuit voltage (V_{OC}) of 1.16 V, a short-circuit current density (J_{SC}) of 20.03 mA cm^{-2}, and a fill factor (FF) of 0.74. In contrast, the performance of the target device is comprehensively improved, delivering a champion PCE of 19.01%, a higher V_{OC} of 1.17 V, a J_{SC} of 21.09 mA cm^{-2}, and an FF of 0.77. Meanwhile, the target devices also exhibit restricted J-V hysteresis between forward scan and reverse scan relative to that of the control device, suggesting the suppression of ion migration.[39] The calculated hysteresis index of the target device, as shown in Figure 3d is 0.03, which is greatly lower than that of the control device (0.11).[39,40] Figure 3e further shows PCE distributions of 20 parallel devices to confirm the enhancements and reproducibility of PQD solar cells. The device parameters for statistics are shown in Figure S14 and Table S6 (Supporting Information). The improved J_{SC} in the target device is also reflected in its high external quantum efficiency (EQE) (Figure 3f). The target device exhibits higher EQE response in the region from 400–800 nm, suggesting more efficient charge dissociation and transport, which may be attributed to the enhanced electronic coupling and surface passivation. The integrated J_{SC} for the target device is 20.26 mA

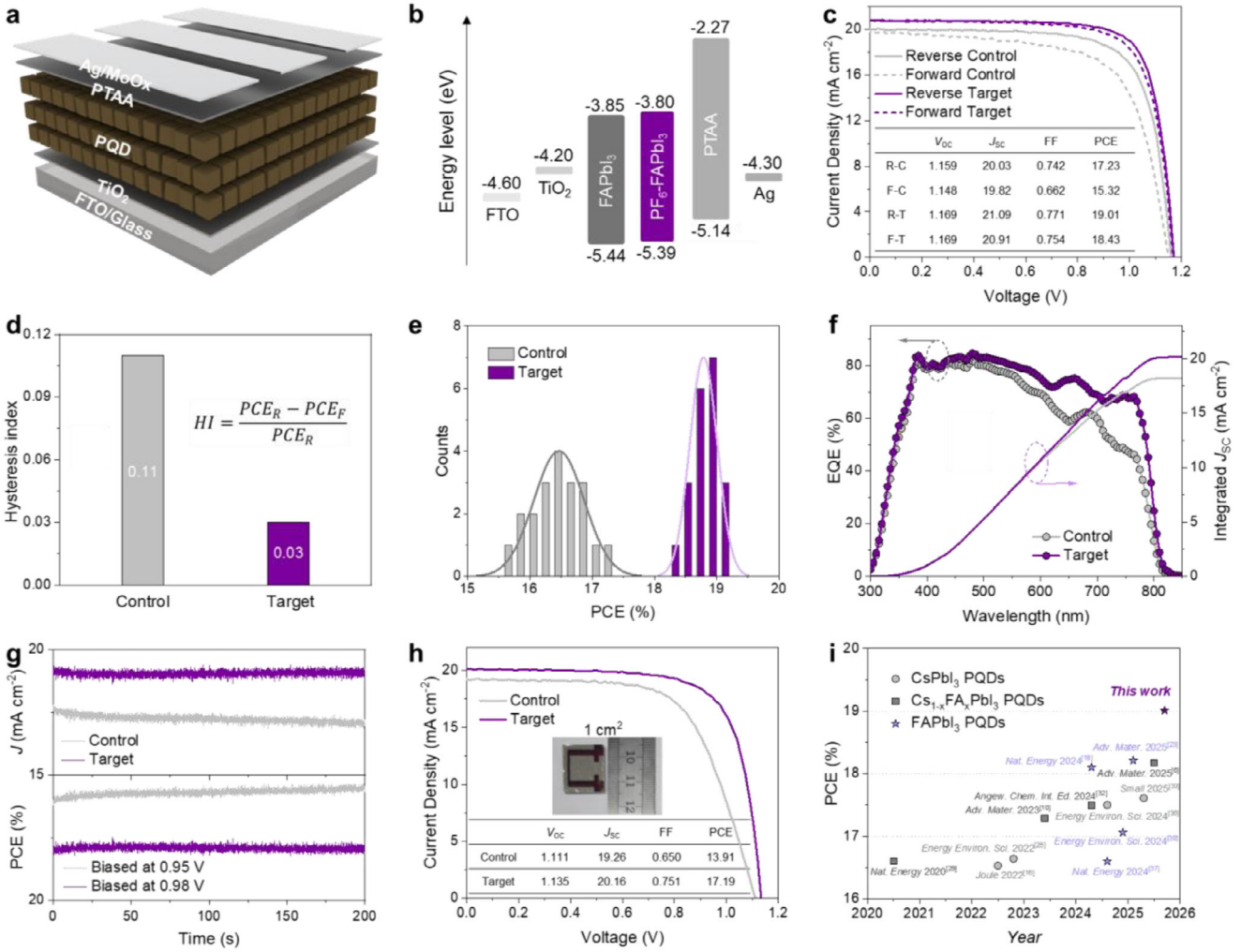

Figure 3. a) Device structure of $FAPbI_3$ PQD solar cell. b) Energy level diagram of PQD solar cells. c) *J–V* curves of the control and target PQD solar cells under reverse and forward scanning direction. d) Calculated hysteresis index of the control and target PQD solar cells. e) Statistical PCEs, f) EQE spectrum, and g) SPO of the control and target PQD solar cells. h) *J–V* curves of the control and target PQD solar cells in 1 cm^2 device area. i) Summary of recently reported high efficiency PQD solar cells with PCE over 16.5%.

cm^{-2}, which is higher than the control device (18.15 mA cm^{-2}). Meanwhile, the stabilized power output (SPO; Figure 3g) of these devices verified the reliability of *J–V* measurements, where the target device shows a stabilized PCE of 18.69%, higher than that of the control device (16.26%). Furthermore, $MAPF_6$-PQD was employed in 1 cm^2-area solar cells as shown in Figure 3h, achieving an efficiency of 17.19%, outperforming the control device (PCE = 13.91%). Moreover, we further introduced MAI and $MABF_4$ into $FAPbI_3$ PQDs for comparison regarding anion specificity. Both MAI and $MABF_4$ boost $FAPbI_3$ PQD device efficiency, but only $MABF_4$ significantly suppresses hysteresis, as shown in Figure S15 (Supporting Information). This confirms that large-sized fluorinated anions (like BF_4^- and PF_6^-) uniquely mitigate ion migration while enhancing performance. This fluorinated pseudo-halide strategy was also applied in $MAPbI_3$ PQDs, and the results showed an enhanced performance (Figure S16, Supporting Information), indicating the universality of this strategy. As summarized in Figure 3i, in comparison with the recently reported high-efficiency (>16.5%) PQD solar cells, we reported the target modification of $FAPbI_3$ PQD surfaces, which enables further enhanced PCE exceeding 19% and achieves the record-high efficiency for PQD photovoltaic.

To assess the long-term stability of PQD films and devices, systematic evaluations were conducted under different operational and environmental stress conditions. **Figure** 4a displays the stability of unencapsulated devices under the N_2 condition at different storage times. The target device maintains over 93% of its initial efficiency after ageing 1000 h, whereas that of the control device retains ≈77% of its original PCE. Moreover, the hydrophobic F atom in $MAPF_6$ is conducive to isolating water in the environment and inhibiting the structural degradation of PQDs. The water contact angle measurements (Figure S17, Supporting Information) indicate a more hydrophobic property of target PQDs. Therefore, the long-term stability of unencapsulated PQD solar cells tracked under environmental conditions (relative humidity of 25–30% and temperature of 25 °C, Figure 4b) shows the PCE of

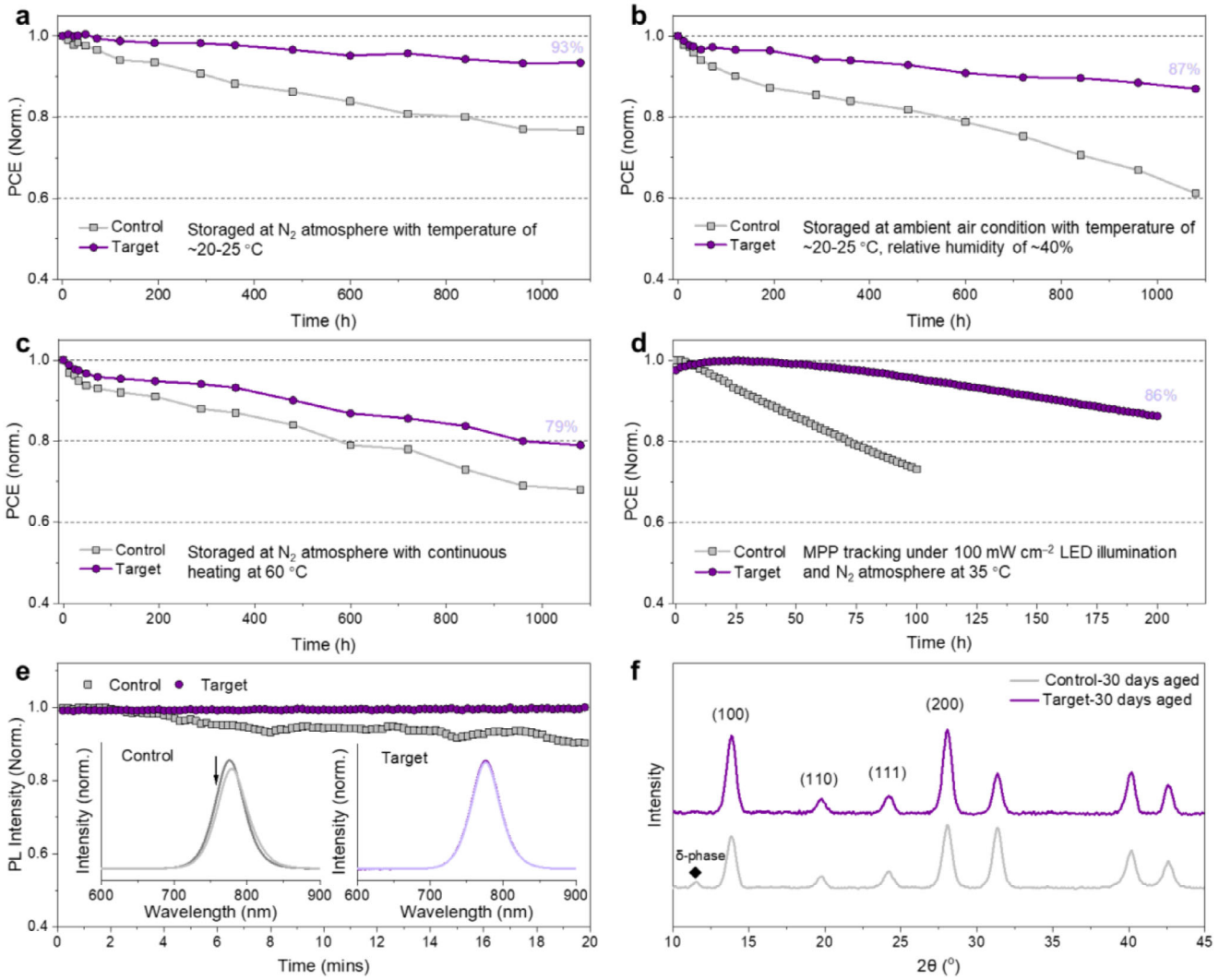

Figure 4. Storage stability of different PQD solar cells in a) N_2, b) ambient air, and c) heating conditions. d) MPP operational stability of different PQD solar cells. e) PL stability of different PQD films under continuous lighting. f) Structure stability of different PQD films tracked by XRD characterization.

the control device decreased to 60% of the original PCE after 1000 h, while the target device maintains about ≈90% of the initial PCE, showing better environmental storage stability. Figure 4c further demonstrates the improvement in the thermal stability of devices, and the target device maintains ≈80% of its initial PCE after 1000 h of storage under the condition of continuous heating at 60 °C in a N_2 environment, suggesting effective passivation of the PQD layers by PF_6^- ions. In contrast, the control device shows over 70% degradation under the same aging conditions. Finally, in the maximum power point tracking (MPP) (exposed to continuous 1-sun illumination in a N_2 environment with a temperature of ≈35 °C), the target device demonstrates stable PCE after 200 h and maintains 86% of its initial efficiency (Figure 4d). Under the same conditions, the efficiency of the control device degraded to ≈70% after 100 h of aging. The enhanced operational stability further suggests the improved stability of PQD films and the suppression of ion migration.[41]

In addition, to more comprehensively assess the impact of the light source on stability, after exposure to UV light (365 nm, 100 mW cm^{-2}) under environmental conditions (relative humidity of 25–30% and temperature of 25 °C), the stability of the control and target films were monitored by in situ PL characterization, with results shown in Figure 4e. The control film exhibits 9% PL intensity reduction accompanied by a ≈2 nm redshift in the emission peak after 30 min of illumination, indicative of photoinduced structural degradation and nanocrystal aggregation. In contrast, the target film retains 98% of its initial PL intensity with negligible spectral shifting (<0.3 nm), demonstrating exceptional photostability.[42] Meanwhile, we monitored the structural stability of the PQD film (relative humidity of 25–30% and temperature of 25 °C) shown in Figure 4f. The XRD results indicate that the target film well maintains its initial perovskite structure that after aging 30 days, while a distinct peak emerged at 11.5° (2θ) belongs to δ-phase in the control PQDs.

Finally, to elucidate the mechanism behind enhanced efficiency and stability, a set of device characterizations was conducted. As shown in **Figure 5**a, space charge limited current (SCLC) measurement reveals a considerable reduction in

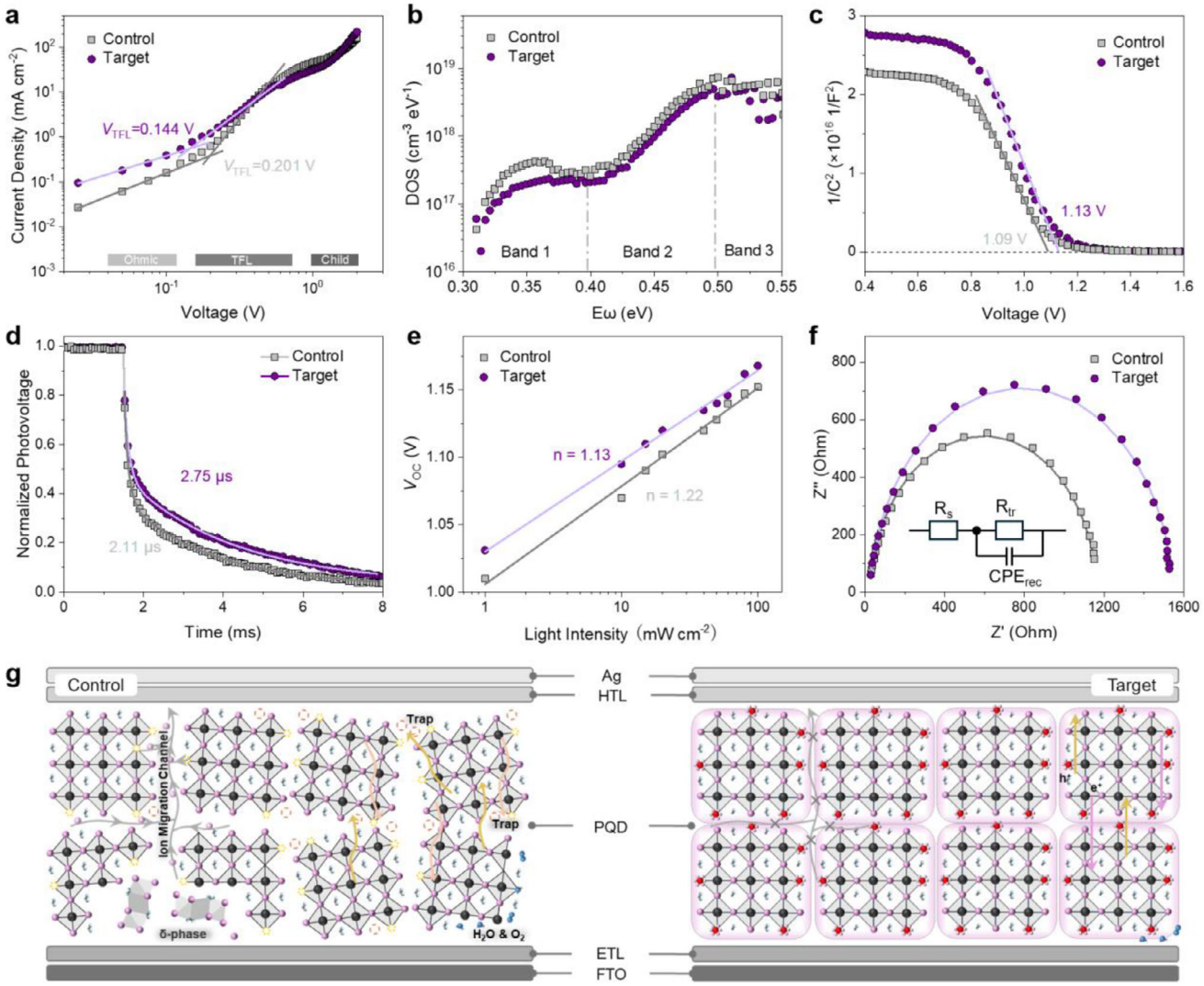

Figure 5. a) SCLC curves for electron-only devices. b) tDOS calculated from the frequency-dependent capacitance measurements. c) C–V curves, d) TPV decay spectra, e) light intensity dependence, and f) Nyquist plots of the control and target PQD devices. g) Schematic of ion migration, charge carrier extraction, and stability of the control and target PQD devices.

trap-filled limit voltage (V_{TFL}) for the target device (0.144 V) compared to the control device (0.201 V), corresponding to a decreased trap-state density from 1.16×10^{16} cm^{-3} to 0.83×10^{16} cm^{-3}.[43] Trap density-of-states (tDOS) analysis further shows uniformly lower trap densities across all energy depths in the target devices, particularly for shallow traps (Region I) associated with surface defects (Figure 5b).[44] Capacitance-voltage (C–V) profiling demonstrates a higher built-in potential (V_{bi} = 1.13 V) in the target device (Figure 5c), which could enhance charge extraction efficiency and mitigate interfacial charge accumulation. Moreover, *J*–*V* characteristics under dark conditions (Figure S18, Supporting Information) reveal a significant suppression of dark current in the target devices relative to the control one.[45] Transient photovoltage (TPV) measurements were performed to probe charge carrier dynamics (Figure 5d). Bi-exponential fitting (Table S7, Supporting Information) reveals a prolonged carrier lifetime of 2.75 μs for the target device (2.11 μs for the control device), which may be attributed to surface passivation and suppressed non-radiative recombination.[46] Similarly, power-law fitting of J_{SC} (Figure S19, Supporting Information) shows $\alpha = 0.99$ for the target device and 0.98 for the control one, indicating suppressed bimolecular recombination and enhanced charge collection efficiency. Light intensity-dependent V_{OC} analysis (Figure 5e) shows an ideality factor of 1.22 and 1.13 for control and target devices, respectively. The near-unity ideality factor in the target device suggests reduced trap-assisted Shockley–Read–Hall (SRH) recombination.[47] Electrochemical impedance spectroscopy (EIS) further validated these findings, with the target device exhibiting lower series resistance (R_s) and higher recombination resistance (R_{tr}) (Figure 5f; Table S8, Supporting Information), demonstrating improved interfacial charge transfer and reduced carrier recombination.[48] To verify the suppression of ion migration, we conducted additional variable temperature EIS measurements on PQD devices treated with or without $MAPF_6$

under 1 sun and 0 V applied bias as shown in Figure S20 (Supporting Information). The ion migration activation energy (E_a) of the control device and the target device are calculated to be 0.27 and 0.31 eV, respectively, confirming an increased energy barrier of ion migration in the PF_6-treated PQD devices.[49]

Based on these findings, we propose a mechanistic model to explain how $MAPF_6$ ligand engineering enhances device performance and stability by modifying the surface properties of PQDs. As shown in Figure 5g, during antisolvent treatment, removal of long-chain OA/OAm ligands creates surface vacancies, which act as trap states, accelerate moisture/oxygen ingress, and degrade photovoltaic performance and stability. Additionally, the incomplete surface structure disrupts the preferred orientation of PQD films, increases roughness, and impedes charge transport. $MAPF_6$ treatment addresses these issues by replacing OAm with MA cations and OA with PF_6^- anions. This ionic ligand stabilizes the PQD surface, restores structural integrity, and could also promote long-range order in the PQD film. Consequently, the target film exhibits suppressed trap-assisted non-radiative recombination and enhanced carrier transport, leading to improved photovoltaic performance. Furthermore, the large size of PF_6^- and the hydrophobicity of F atoms significantly mitigate ion migration and water/oxygen invasion, enhancing the long-term stability under light and thermal stresses.

3. Conclusion

In summary, we reported a facile method to modulate the surface of $FAPbI_3$ PQDs using a multifunctional ligand PF_6^-, which can simultaneously manage the charge transport and structural integrity in PQD toward high efficiency and durable solar cells. By replacing the long-chain capping ligands, the short PF_6^- ligand effectively passivates iodide vacancies and suppresses trap states. Meanwhile, the compact ligand shell formed by PF_6^- could minimize inter-dot spacing toward enhanced electronic coupling. Furthermore, the steric bulk of PF_6^- would act as a physical barrier at PQD interfaces to suppress ion migration. Consequently, the target PQD solar cell devices output a best PCE of over 19.01%, and 17.19% efficiency in 1 cm^2-sized devices. More importantly, the hydrophobicity and lattice anchoring of PF_6^- enhanced the stability of the PQD device, with a retention rate of 90% after 1000 h under ambient conditions and ≈90% under 200 h of continuous illumination. These findings and joint advancement in efficiency and stability represent a robust surface engineering strategy that collaborates to improve optoelectronic performance and environmental resilience, advancing PQD photovoltaics toward realistic applications.

4. Experimental Section

Synthesis of $FAPbI_3$ PQDs: $FAPbI_3$ PQDs were synthesized as described in previous reports with slight modification.[17] First, the FA-precursor was prepared by mixing FAAc (512 mg) and OA (10 mL) in a 50 mL three-neck flask and stirring under vacuum conditions for 30 min at 40 °C. Then, the flask was heated up to 80 °C with N_2 atmosphere and kept for 1 h. Subsequently, 516 mg of PbI_2 and 40 mL of ODE were added into a 250 mL three-neck flask and degassed at 90 °C for 1 h. Subsequently, 6 mL of OA and 3 mL of OAm were injected into the reaction mixture under a N_2 atmosphere. The mixture was degassed under vacuum until the reaction mixture became clear. Finally, the temperature of the reaction mixture was decreased to 80 °C under N_2 flow, and 6 mL of FA-precursor solution was rapidly injected into the flask. After 5–10 s, the reaction mixture was then quickly cooled in an ice-water bath.

Surface Treatment of $FAPbI_3$ PQDs: The crude solution of $FAPbI_3$ PQDs (55 mL) was equally divided into two tubes and centrifuged at 12 000 rpm for 5 min. After discarding the supernatant, the PQD solids were redispersed in 6 mL of hexane. For the control PQDs, 10 mL of MeOAc was added into each tube and centrifuged at 12 000 rpm for 3 min. For $MAPF_6$-treated PQDs, 10 mL of MeOAc solution dissolved with $MAPF_6$ (concentration of 0.01, 0.05, 0.1, or 0.2 mg mL^{-1}) was added into each tube and centrifuged at 12 000 rpm for 3 min, respectively. After discarding supernatant, the PQD solids were dried and redispersed in n-octane to prepare the PQD solution with a concentration of 100 mg mL^{-1} for film deposition.

Device Fabrication and Characterizations: The FTO glass substrate was continuously ultrasonically cleaned in acetone, deionized water, acetone, and IPA. Then, the FTO substrate was treated with UV ozone for 30 min. A compact TiO_2 electron transport layer ≈40 nm thick was prepared on the substrate by the chemical bath deposition method. Before depositing PQD films, the TiO_2 film was annealed at 200 °C for 30 min and treated with UV ozone for 15 min. For post-treatment, an IPA solution dissolved with MAI (3 mg mL^{-1}) was used as the ligand solution, as previously reported.[18] The PQD solution was spin-coated onto the TiO_2 film at 1000 rpm for 10 s, followed by a speed of 2000 rpm for 5 s. Subsequently, the PQD film was soaked in the ligand solution for 5 s and then spin dried. This process is repeated 4 times to obtain the required thickness of the PQD films. The PQD film deposition process was carried out under environmental conditions with ≈20% humidity. Subsequently, 15 mg mL^{-1} PTAA of toluene solution doped by tris(pentafluorophenyl)borane (LAD) was spin-coated on PQD film to deposit the hole transport layer. Finally, MoO_3 (8 nm) and Ag (120 nm) electrodes were deposited by thermal evaporation.

Supporting Information

Supporting Information is available from the Wiley Online Library or from the author.

Acknowledgements

C.Z. and D.L. contributed equally to this work. This work was financially supported by the National Key Research and Development Program of China (No. 2023YFE0210000), the National Natural Science Foundation of China (No. 52261145696, 52473187, and 22405186), Natural Science Foundation of Jiangsu Province (BK20240763), "111" project, Collaborative Innovation Center of Suzhou Nano Science and Technology, Soochow University, T.W. acknowledges the support of the Hong Kong Innovation and Technology Commission (MHP/233/23).

Conflict of Interest

The authors declare no conflict of interest.

Data Availability Statement

The data that support the findings of this study are available from the corresponding author upon reasonable request.

Keywords

high efficiency, perovskite quantum dot, pseudo-halide anion, solar cells, stability

Received: June 26, 2025
Revised: July 28, 2025
Published online:

[1] Q. A. Akkerman, G. Rainò, M. V. Kovalenko, L. Manna, *Nat. Mater.* **2018**, *17*, 394.
[2] M. V. Kovalenko, *Nat. Nanotechnol.* **2015**, *10*, 994.
[3] X. Sun, L. Yuan, Y. Liu, G. Shi, Y. Wang, C. Liu, X. Zhang, Y. Zhao, C. Zhao, M. Ma, B. Shen, Y. Wang, Q. Shen, Z. Liu, W. Ma, *Nat. Synth.* **2025**, *4*, 167.
[4] A. Swarnkar, A. R. Marshall, E. M. Sanehira, B. D. Chernomordik, D. T. Moore, J. A. Christians, T. Chakrabarti, J. M. Luther, *Science* **2016**, *354*, 92.
[5] "Best Research-Cell Efficiency Chart | Photovoltaic Research | NREL" can be found under https://www.nrel.gov/pv/cell-efficiency, (accessed: June 2025).
[6] G. Wang, B. Ren, X. Mei, M. Zhang, J. Qiu, Z. Sun, X. Zhang, *Adv. Mater.* **2025**, https://doi.org/10.1002/adma.202508425.
[7] J. Yuan, A. Hazarika, Q. Zhao, X. Ling, T. Moot, W. Ma, J. M. Luther, *Joule* **2020**, *4*, 1160.
[8] X. Zhang, H. Huang, C. Zhao, J. Yuan, *Chem. Soc. Rev.* **2025**, *54*, 3017.
[9] A. Hazarika, Q. Zhao, E. A. Gaulding, J. A. Christians, B. Dou, A. R. Marshall, T. Moot, J. J. Berry, J. C. Johnson, J. M. Luther, *ACS Nano* **2018**, *12*, 10327.
[10] D. Jia, J. Chen, R. Zhuang, Y. Hua, X. Zhang, *Adv. Mater.* **2023**, *35*, 2212160.
[11] Y. Zhang, T. D. Siegler, C. J. Thomas, M. K. Abney, T. Shah, A. De Gorostiza, R. M. Greene, B. A. Korgel, *Chem. Mater.* **2020**, *32*, 5410.
[12] L. Protesescu, S. Yakunin, M. I. Bodnarchuk, F. Krieg, R. Caputo, C. H. Hendon, R. X. Yang, A. Walsh, M. V. Kovalenko, *Nano Lett.* **2015**, *15*, 3692.
[13] S. Ding, M. Hao, C. Fu, T. Lin, A. Baktash, P. Chen, D. He, C. Zhang, W. Chen, A. K. Whittaker, Y. Bai, L. Wang, *Adv. Sci.* **2022**, *9*, 2204476.
[14] J. De Roo, M. Ibáñez, P. Geiregat, G. Nedelcu, W. Walravens, J. Maes, J. C. Martins, I. Van Driessche, M. V. Kovalenko, Z. Hens, *ACS Nano* **2016**, *10*, 2071.
[15] J. Xue, J.-W. Lee, Z. Dai, R. Wang, S. Nuryyeva, M. E. Liao, S.-Y. Chang, L. Meng, D. Meng, P. Sun, O. Lin, M. S. Goorsky, Y. Yang, *Joule* **2018**, *2*, 1866.
[16] D. Jia, J. Chen, J. Qiu, H. Ma, M. Yu, J. Liu, X. Zhang, *Joule* **2022**, *6*, 1632.
[17] X. Zhang, H. Huang, L. Jin, C. Wen, Q. Zhao, C. Zhao, J. Guo, C. Cheng, H. Wang, L. Zhang, Y. Li, Y. Maung Maung, J. Yuan, W. Ma, *Angew. Chem., Int. Ed.* **2023**, *62*, 202214241.
[18] H. Aqoma, S.-H. Lee, I. F. Imran, J.-H. Hwang, S.-H. Lee, S.-Y. Jang, *Nat. Energy.* **2024**, *9*, 324.
[19] M. Zhang, X. Mei, G. Wang, J. Qiu, Z. Sun, X. Zhang, *Energy Environ. Sci.* **2024**, *18*, 300.
[20] H. Song, J. Yang, W. H. Jeong, J. Lee, T. H. Lee, J. W. Yoon, H. Lee, A. J. Ramadan, R. D. J. Oliver, S. C. Cho, S. G. Lim, J. W. Jang, Z. Yu, J. T. Oh, E. D. Jung, M. H. Song, S. H. Park, J. R. Durrant, H. J. Snaith, S. U. Lee, B. R. Lee, H. Choi, *Adv. Mater.* **2023**, *35*, 2209486.
[21] H. Zai, Y. Ma, Q. Chen, H. Zhou, *J. Energy Chem.* **2021**, *63*, 528.
[22] M. Xie, J. Guo, X. Zhang, C. Bi, X. Sun, H. Li, L. Zhang, D. Binks, G. Li, W. Zheng, J. Tian, *Adv. Funct. Mater.* **2023**, *33*, 2300116.
[23] D. Li, C. Zhao, X. Zhang, X. Zhao, H. Huang, H. Li, F. Li, J. Yuan, *Adv. Mater.* **2025**, *37*, 2417346.
[24] L. M. Wheeler, E. M. Sanehira, A. R. Marshall, P. Schulz, M. Suri, N. C. Anderson, J. A. Christians, D. Nordlund, D. Sokaras, T. Kroll, S. P. Harvey, J. J. Berry, L. Y. Lin, J. M. Luther, *J. Am. Chem. Soc.* **2018**, *140*, 10504.
[25] D. Jia, J. Chen, R. Zhuang, Y. Hua, X. Zhang, *Energy Environ. Sci.* **2022**, *15*, 4201.
[26] J. Fu, S. Chen, L. Yuan, Q. Pan, Z. Liu, J. Chen, P. Xu, Q. Zhang, M. Cao, *J. Phys. Chem. C* **2024**, *128*, 20641.
[27] J. Chen, S.-G. Kim, N.-G. Park, *Adv. Mater.* **2018**, *30*, 1801948.
[28] J. Tao, X. Liu, J. Shen, S. Han, L. Guan, G. Fu, D.-B. Kuang, S. Yang, *ACS Nano* **2022**, *16*, 10798.
[29] M. Hao, Y. Bai, S. Zeiske, L. Ren, J. Liu, Y. Yuan, N. Zarrabi, N. Cheng, M. Ghasemi, P. Chen, M. Lyu, D. He, J.-H. Yun, Y. Du, Y. Wang, S. Ding, A. Armin, P. Meredith, G. Liu, H.-M. Cheng, L. Wang, *Nat. Energy* **2020**, *5*, 79.
[30] M. Zhang, Q. Gao, X. Mei, J. Qiu, R. Zhuang, Y. Hua, Z. Sun, X. Zhang, *Energy Environ. Sci.* **2024**, *17*, 2145.
[31] R. Wang, J. Ni, S. Zhang, M. Yan, H. Li, X. Song, G. Li, Y. Zhang, J. Li, H. Cai, J. Zhang, *Sol. Energy Mat. Sol. C* **2025**, *290*, 113722.
[32] G. Wang, Y. Sun, M. Zhang, X. Mei, Z. Sun, X. Zhang, *Angew. Chem., Int. Ed.* **2025**, *64*, 202416747.
[33] X. Mei, B. Ren, J. Qiu, Z. Sun, X. Zhang, *Small* **2025**, *21*, 2504748.
[34] Z. Li, B. Li, X. Wu, S. A. Sheppard, S. Zhang, D. Gao, N. J. Long, Z. Zhu, *Science* **2022**, *376*, 416.
[35] J. Guo, B. Wang, J. Min, J. Shi, Y. Wang, X. Ling, Y. Shi, I. Ullah, D. Chu, W. Ma, J. Yuan, *ACS Nano* **2024**, *18*, 19865.
[36] H. Li, H. Huang, D. Li, X. Zhang, C. Zhao, X. Zhao, W. Ma, J. Yuan, *Energy Environ. Sci.* **2024**, *18*, 972.
[37] X. Zhang, H. Huang, C. Zhao, L. Jin, C. Lee, Y. Li, D.-H. Ko, W. Ma, T. Wu, J. Yuan, *Nat. Energy* **2024**, *9*, 1378.
[38] J. Chen, L. Ye, T. Wu, Y. Hua, X. Zhang, *Adv. Mater.* **2024**, *36*, 2404495.
[39] J. Chen, D. Lee, N.-G. Park, *ACS Appl. Mater. Interfaces* **2017**, *9*, 36338.
[40] Z. Zhang, W. Chen, X. Jiang, J. Cao, H. Yang, H. Chen, F. Yang, Y. Shen, H. Yang, Q. Cheng, X. Chen, X. Tang, S. Kang, X. Ou, C. J. Brabec, Y. Li, Y. Li, *Nat. Energy* **2024**, *9*, 592.
[41] D. He, D. Ma, J. Zhang, Y. Yang, J. Ding, C. Liu, X. Liu, Y. Yu, T. Liu, C. Chen, M. Li, J. Chen, *Adv. Mater.* **2025**, https://doi.org/10.1002/adma.202505115.
[42] C. Zhao, C. Cazorla, X. Zhang, H. Huang, X. Zhao, D. Li, J. Shi, Q. Zhao, W. Ma, J. Yuan, *J. Am. Chem. Soc.* **2024**, *146*, 4913.
[43] J. Guo, G. Meng, X. Zhang, H. Huang, J. Shi, B. Wang, X. Hu, J. Yuan, W. Ma, *Adv. Mater.* **2023**, *35*, 2302839.
[44] X. Zheng, B. Chen, J. Dai, Y. Fang, Y. Bai, Y. Lin, H. Wei, X. C. Zeng, J. Huang, *Nat. Energy* **2017**, *2*, 1.
[45] Z. Ni, C. Bao, Y. Liu, Q. Jiang, W.-Q. Wu, S. Chen, X. Dai, B. Chen, B. Hartweg, Z. Yu, Z. Holman, J. Huang, *Science* **2020**, *367*, 1352.
[46] Q. Jiang, Y. Zhao, X. Zhang, X. Yang, Y. Chen, Z. Chu, Q. Ye, X. Li, Z. Yin, J. You, *Nat. Photonics* **2019**, *13*, 460.
[47] F. Li, X. Zhang, J. Shi, L. Jin, J. Qiao, J. Guo, H. Yin, Y. Li, J. Yuan, W. Ma, *Adv. Funct. Mater.* **2023**, *33*, 2302542.
[48] Y. Wu, Q. Wang, Y. Chen, W. Qiu, Q. Peng, *Energy Environ. Sci.* **2022**, *15*, 4700.
[49] Z. Zhang, W. Chen, X. Jiang, J. Cao, H. Yang, H. Chen, F. Yang, Y. Shen, H. Yang, Q. Cheng, X. Chen, X. Tang, S. Kang, X. Ou, C. J. B., Y. Li, Y. Li, *Nat. Energy* **2024**, *9*, 592.